



Compositional inhomogeneity and its effect on the hardness of nanostructured refractory high-entropy alloys

Chunyang Wang^a, Mingde Qin^b, Tianjiao Lei^c, Liyang Wan^a, Sashank Shivakumar^b, Kim Kisslinger^e, Timothy J. Rupert^{c,d}, Jian Luo^b, Huolin L. Xin^{a,*}

^a Department of Physics and Astronomy, University of California Irvine, Irvine, CA 92697, USA

^b Department of NanoEngineering, Program of Materials Science and Engineering, University of California San Diego, La Jolla, CA 92093, USA

^c Department of Materials Science and Engineering, University of California Irvine, Irvine, CA, 92697, USA

^d Department of Mechanical and Aerospace Engineering, University of California Irvine, Irvine, CA, 92697, USA

^e Center for Functional Nanomaterials, Brookhaven National Laboratory, Upton, NY 11973, USA

ARTICLE INFO

Keywords:

Nanocrystalline metal
Microstructure
Sintering
Mechanical properties
Scanning/transmission electron microscopy (STEM)

ABSTRACT

The pronounced compositional inhomogeneity observed in refractory high-entropy alloys (HEAs), as opposed to non-refractory HEAs, has an important influence on their mechanical properties, thereby posing a significant challenge for the development of high-performance refractory HEAs. In this work, by combining transmission electron microscopy imaging, chemical analysis, and nano-hardness tests, we investigate the compositional inhomogeneities in a series of sintered nanostructured HEAs and elucidate their influence on the material's hardness. We reveal that the compositional inhomogeneity of the sintered nanostructured HEAs is temperature- and component-dependent. By correlating the hardness of nanostructured HEAs to the evolving compositional inhomogeneity, our work demonstrates that the compositional inhomogeneity in nanostructured HEAs can be tuned by sintering temperature or alloying towards optimized microstructure and hardness.

1. Introduction

High-entropy alloys (HEAs), since the pioneering work done by Cantor et al. [1] and Yeh et al. [2,3] in 2004, have generated considerable interest because their unconventional chemical structures hold great promise for achieving unprecedented properties such as high hardness [4,5], high strength [6–12], and good thermal stability [13]. By tuning the elemental distribution at different length scales, the microstructure and architecture of HEAs could be altered towards optimized mechanical properties and applications [14–17]. For example, it has been demonstrated that by tuning the inherent chemical inhomogeneity at the atomic scale, the degree of the chemical short-range ordering (SRO) in HEAs could be tailored and thus has an important influence on the mechanical performance of HEAs [18–22]. Compared with the atomic-scale chemical fluctuation which has been extensively studied, the compositional heterogeneity at larger length scale (e.g., grain scale) and its influence on the mechanical performance are less studied.

Compared to non-refractory HEAs, refractory HEAs [23–26] which contain elements with high melting points usually show more prominent

compositional inhomogeneity such as phase separation due to disparate melting points of different components [27–30]. To find effective strategies to regulate or to minimize the inhomogeneity is of critical importance to optimizing current refractory HEAs. Routinely, increasing the sintering temperature is an effective way to produced more homogenized refractory HEAs as it promotes diffusion and consolidation [31]. Equally importantly, reducing the grain size of refractory HEAs is another potential avenue to fabricate more homogeneous refractory HEAs with increased surface energy and interdiffusion during sintering. Aside from that, studies have demonstrated that increased amount of grain boundaries can effectively consume radiation defects [32–34], therefore making nanostructured HEAs promising for application in the nuclear industry. Recently, Qin et al. [35] reported simultaneously enhanced sinterability and high-temperature grain-size stability in NbMoTaW-based nanostructured refractory HEAs. Yet, how nanocrystallization influence the intermixing and distribution of the components in the alloy remains obscure. Also, how sintering temperature and elemental alloying [36], two important factors that have been widely explored for refractory HEAs synthesis, influence the compositional inhomogeneity as well as the mechanical performance of

* Corresponding author at: 4129 Frederick Reines Hall, Irvine, CA 92697-4575, USA.

E-mail address: huolin.xin@uci.edu (H.L. Xin).

<https://doi.org/10.1016/j.matchar.2023.113563>

Received 12 September 2023; Received in revised form 6 December 2023; Accepted 12 December 2023

Available online 16 December 2023

1044-5803/© 2023 Elsevier Inc. All rights reserved.

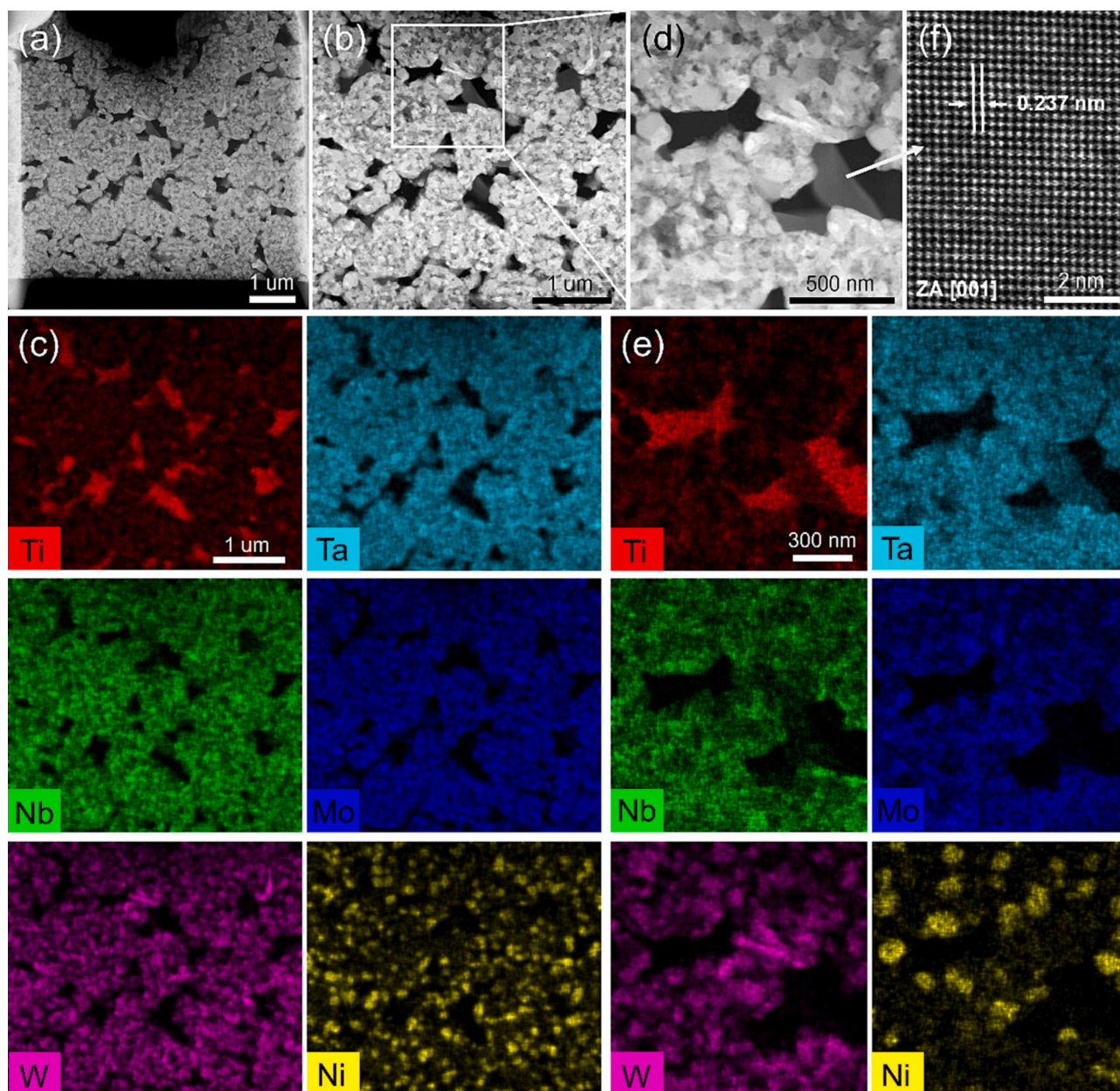


Fig. 1. Structure and chemistry of (TiNbMoTaW)-6Ni sintered at 1300 °C (n-HEA#1). (a) High-angle annular dark-field scanning transmission electron microscopy (HAADF-STEM) image showing the microstructure of n-HEA#1. (b,c) HAADF-STEM image and corresponding energy-dispersive spectroscopic (EDS) maps showing the chemical distribution of Ti, Nb, Mo, Ta, W, Ni in n-HEA#1. (d,e) A magnified HAADF-STEM image and corresponding high-resolution EDS maps of the boxed region in (b). (f) Atomic-resolution HAADF-STEM image (obtained along the [001] zone axis) of a representative body-centered cubic (bcc)-type Ta-Nb-rich slab in n-HEA#1.

nanostructured HEAs remains to be answered. In this work, by employing statistical elemental analysis and atomic imaging, we comparatively investigate the state of compositional inhomogeneity in a series of nanostructured refractory HEAs with varied sintering temperature or elemental alloying. We found that the compositional inhomogeneity can be effectively alleviated with increased sintering temperature and elemental alloying/doping. Furthermore, by correlating the chemical and structural analyses to nanohardness measurements, we elucidate how the tuned compositional inhomogeneity contribute to the hardness enhancement in nanostructured HEAs.

2. Materials selection and processing

Three nanostructured HEA specimens, (TiNbMoTaW)-6Ni sintered at

1300 °C (hereafter denoted as n-HEA#1), (TiNbMoTaW)-6Ni sintered at 1400 °C (hereafter denoted as n-HEA#2), and (TiNbMoTaW)-6Ni-5Zr sintered at 1400 °C (hereafter denoted as n-HEA#3), are synthesized by ball milling following by spark plasma sintering (SPS). For each composition, appropriate amounts of Ti, Nb, Mo, Ta, W, Ni and Zr elemental powders (>99.5% purity, ~325 mesh, Alfa Aesar, MA, USA) were weighed out (18.8Ti-18.8Nb-18.8Mo-18.8Ta-18.8W-6Ni and 17.8Ti-17.8Nb-17.8Mo-17.8Ta-17.8W-6Ni-5Zr in atomic %) in batches of 20 g. The powder mixtures were then transferred in a 100 ml polytetrafluoroethylene (PTFE) planetary milling jar with 20 ml of isopropyl alcohol (IPA) and Y₂O₃-stabilized ZrO₂ (YSZ) milling media at a ball-to-powder mass ratio of 10:1. Planetary ball milling was then conducted at 300 rpm for 24 h in a PQN04 mill (Across International LLC, USA). After milling, the powder mixture was dried in a vacuum oven at 75 °C

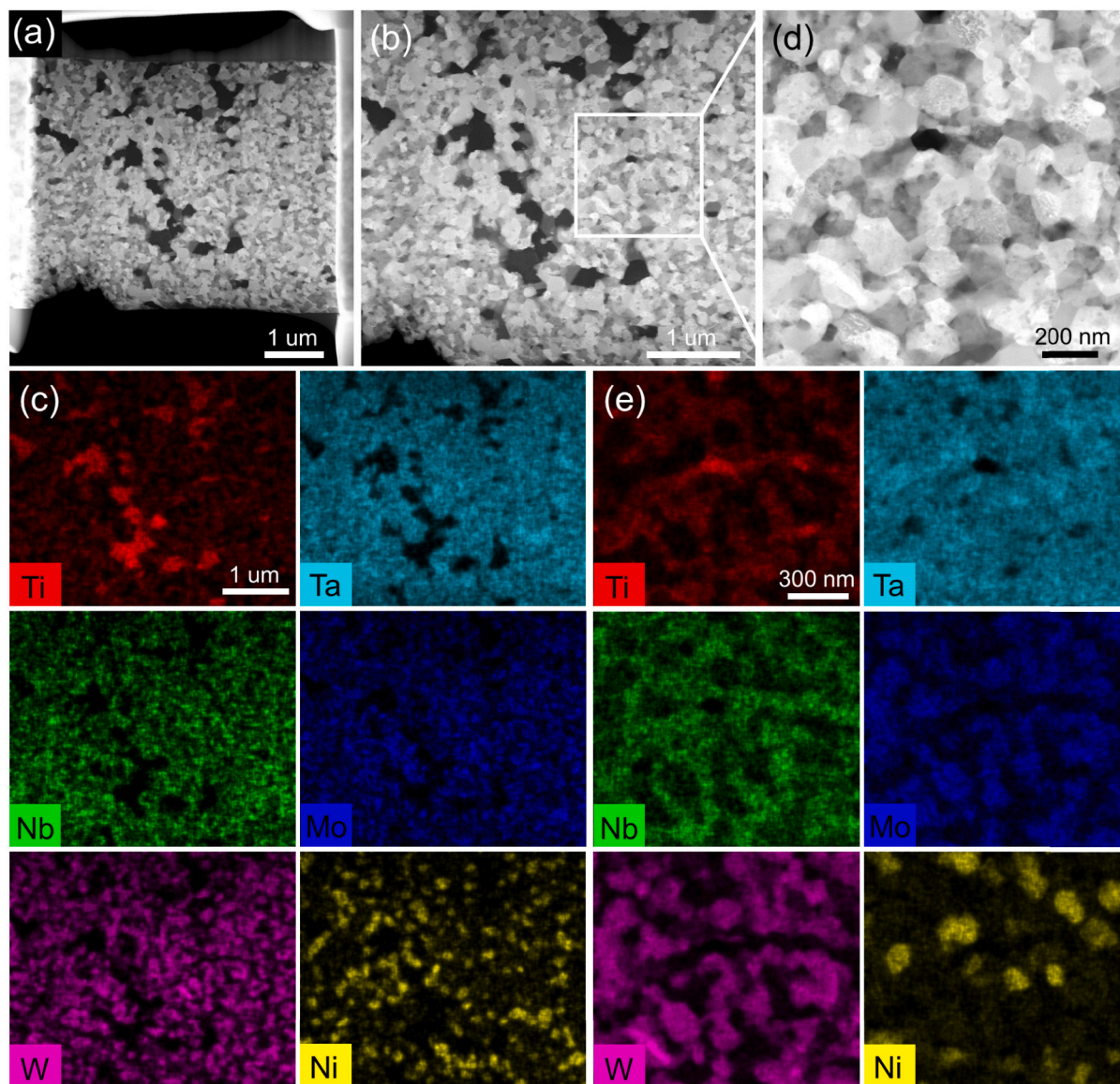


Fig. 2. Structure and chemistry of (TiNbMoTaW)-6Ni sintered at 1400 °C (n-HEA#2). (a) HAADF-STEM image showing the microstructure of n-HEA#2. (b,c) HAADF-STEM image and corresponding EDS maps showing the chemical distribution of Ti, Nb, Mo, Ta, W, Ni in n-HEA#2. (d,e) A magnified HAADF-STEM image of the boxed region in (b) and the corresponding high-resolution EDS maps of the components.

overnight and then immediately transferred into Ar atmosphere (glove box) to prevent oxidation. The milled powders were loaded into 10 mm graphite dies lined with graphite and Mo foils in batches of 3 g, and consecutively consolidated into dense pellets via SPS in vacuum (10^{-2} Torr) using a Thermal Technologies 3000 series SPS (CA, USA). During the SPS, the specimen was first raised to the target temperatures of 1300 °C or 1400 °C at a rate of 100 °C/min, then held isothermally for 5 mins, and eventually cooled down to room temperature by furnace cooling (power off). XRD was performed on an Anton-Paar XRDynamic 500, with a Primalux 3000 Cu source at 40 kV, and a step size of 0.0.01°. Focused-ion beam (FIB) milling (Helios NanoLab) was used to prepare the TEM samples from bulk alloy samples. High-resolution annular dark-field scanning transmission electron microscopy (HAADF-STEM) and high-resolution TEM (HRTEM) imaging were performed on an FEI Talos F200X (scanning) transmission electron microscope operated at the voltage of 200 kV. Energy-dispersive spectroscopy (EDS) experiments were conducted in HAADF-STEM mode with a Super-X EDS detector integrated into the microscope. Berkovich nanohardness tests were

carried out using a diamond indenter with a loading force of 300 mN and a holding time of 10 s. The indentation depth and width are ~ 810 nm and ~ 1.5 μm , respectively. The distance between the nearest two indents is ~ 20 μm . Over 50 measurements were conducted at different locations to ensure statistical validity. Note that hardness measurement depends on many factors such as the loading force, therefore, the absolute hardness value of a specimen may vary from one test condition to another. Yet, since the three samples in our work are tested under the same condition, the relative change of the hardness value is sufficient to indicate the difference of the mechanical properties of the samples.

3. Results

3.1. Microstructural characterization

We investigate the effect of compositional inhomogeneity on the hardness of n-HEAs by combining atomic-resolution TEM imaging, statistical chemical analysis, and nanoindentation tests. Sintering

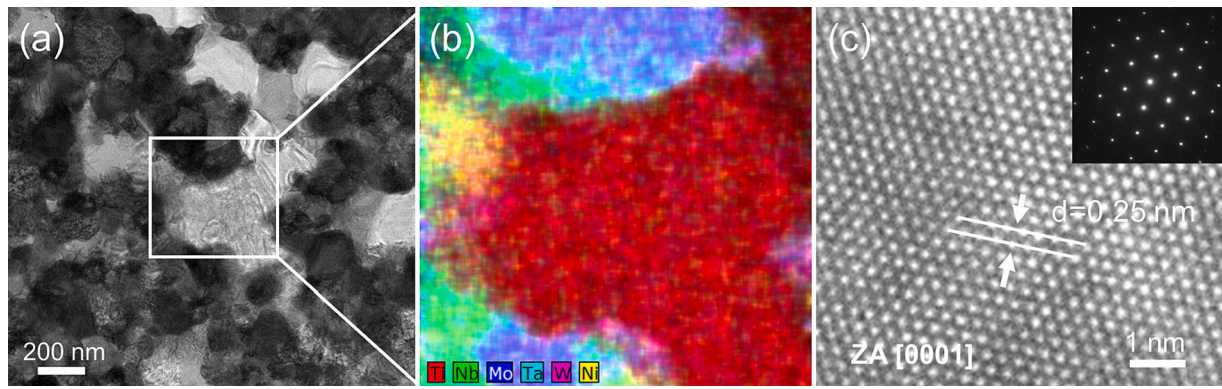


Fig. 3. Structure Ti-rich domains in n-HEA#2. (a,b) Bright-field (BF)-STEM image and an overlapped EDS map of the Ti-rich region corresponding to the boxed region in (a). (c) Atomic-resolution HRTEM image (obtained along the [0001] zone axis of the HCP phase) and electron diffraction pattern (inset) of the Ti-rich domain in (b).

temperature and alloy composition are varied to enable changes in the compositional homogeneity. We adopted relatively low sintering temperatures (1300–1400 °C, which are ~54–57% of the average melting temperatures of Ti, Nb, Mo, Ta, and W) and short sintering duration (5 min), so that the as-sintered n-HEA specimens likely have not been

homogenized (to reach full chemical or thermodynamic equilibria). In addition, since the Ni (6 at.%) and Zr (5 at.%) contents of our alloys (TiNbMoTaW)-6Ni and (TiNbMoTaW)-6Ni-5Zr were designed to be above the solubility limits of five binary systems at 1300 °C, minor secondary phases are formed at the sintering temperatures [35], while

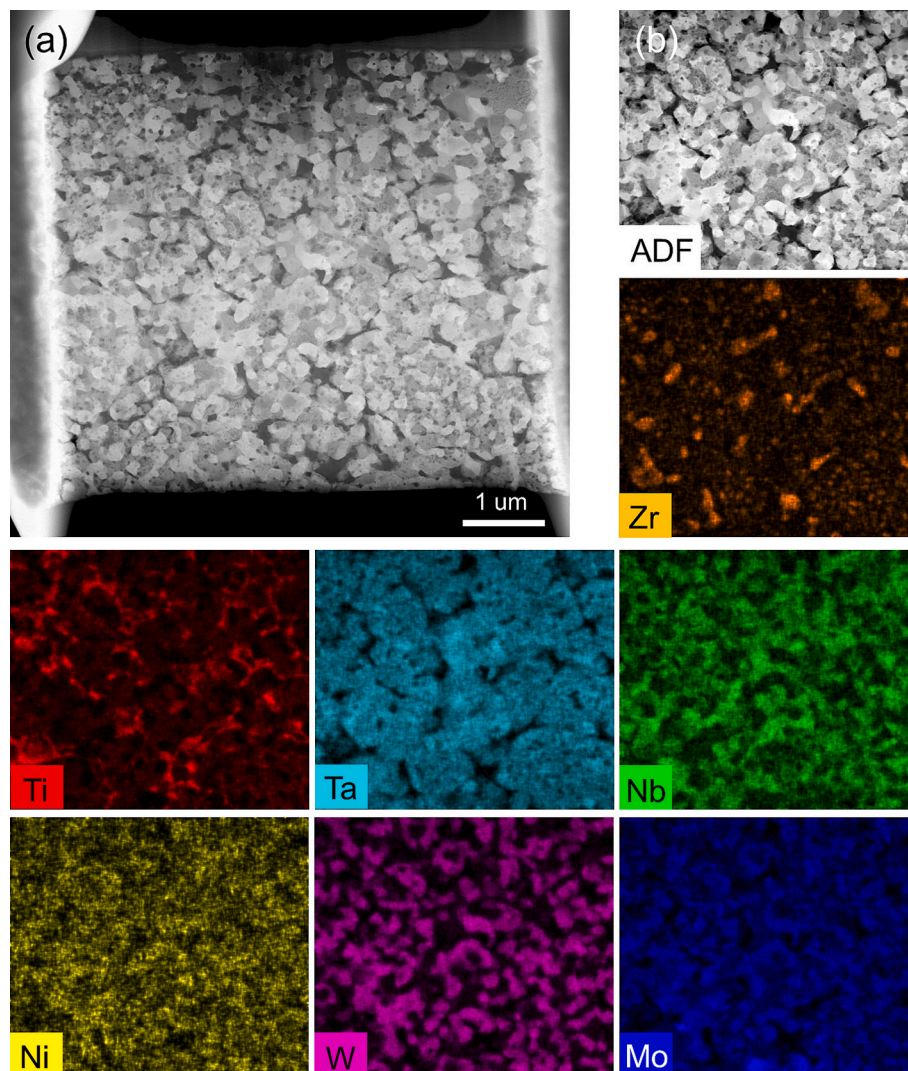


Fig. 4. Structure and chemistry of (TiNbMoTaW)-6Ni-5Zr sintered at 1400 °C (n-HEA#3). (a) HAADF-STEM image showing the microstructure of the n-HEA#3 specimen. (b) EDS maps showing the chemical distribution of Ti, Nb, Mo, Ta, W, Ni, and Zr in n-HEA#3.

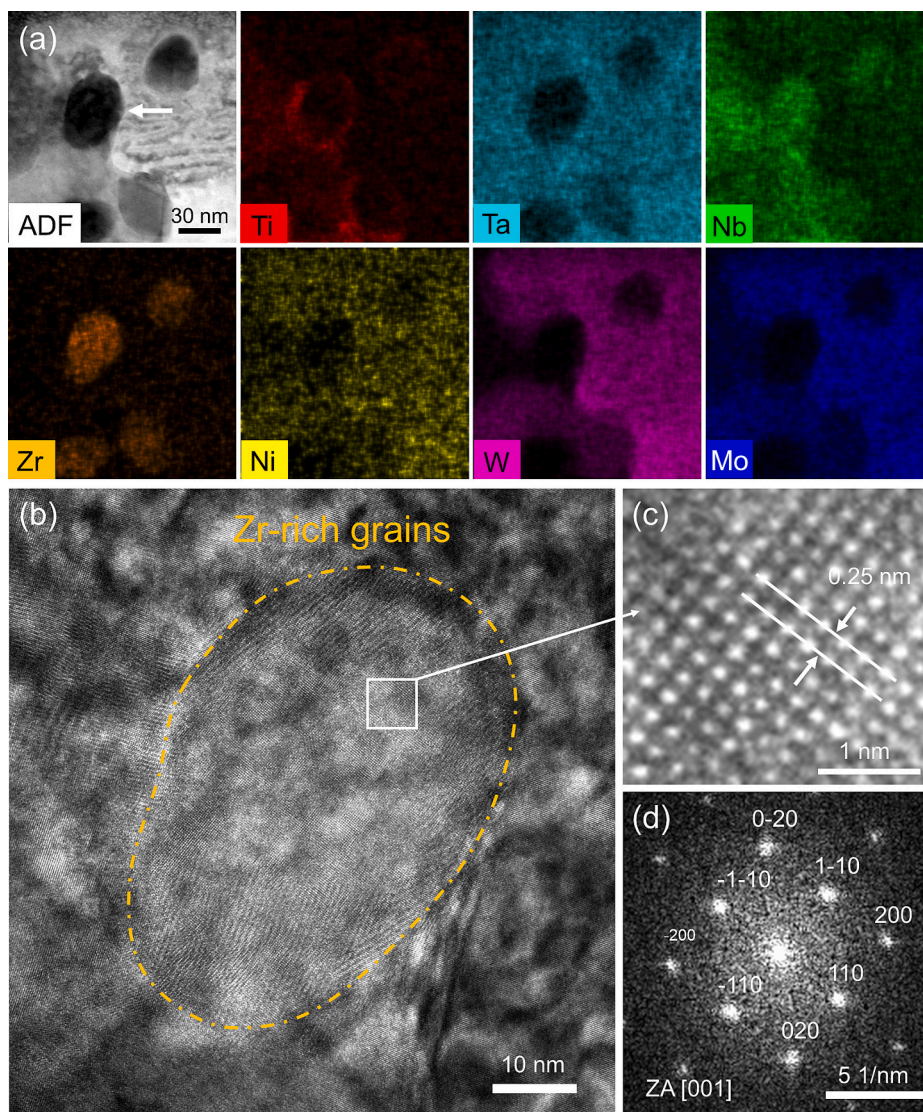


Fig. 5. Structure and chemistry of Zr-rich grains in n-HEA#3. (a) High-resolution EDS maps of Zr-rich near-spherical grains. (b) HRTEM image of the Zr-rich grain indicated by the arrow in (a). (c,d) Enlarged atomic-resolution image and corresponding fast Fourier transform (FFT) of the Zr-rich grain obtained along the [001] zone axis.

all samples exhibit primary BCC structure (see the XRD patterns of the n-HEAs in Fig. S1). Figs. 1a,b present representative HAADF-STEM images of the (TiNbMoTaW)-6Ni (n-HEA#1) sintered at 1300 °C. The result shows that the alloy is composed of bright micro-sized secondary “clusters of grains” (with an average size of 0.9 μm) formed by aggregation of nanocrystalline grains (with an average grain size of 95 nm), separated by discrete dark patches. Since the contrast of a HAADF-STEM image is directly related to the atomic numbers and contrast of the specimen, the dark patches are either composed of low-Z elements or are deficient in mass (e.g., pores/voids). Energy-dispersive spectroscopic (EDS) mapping was further performed to understand the chemical structure of the n-HEA#1 specimen. EDS maps (Fig. 1c) corresponding to the region in Fig. 1b show that the ‘dark’ patches are mainly composed of Ti, while the secondary clusters of grains are composed of Ta, Nb, Mo, W, Ni, Ti. By zooming in, the high-resolution EDS maps (Fig. 1e and Fig. S2) corresponding to the region in Fig. 1d (see BF-TEM image of the same region in Fig. S3) show that Ta-Nb-Ti-rich slabs (indicated by the arrow, see a corresponding atomic-resolution image in Fig. 1f) were also formed next to the Ti-rich patches (see the results from another region in Fig. S4). More importantly, we found that the elemental distribution in the secondary clusters of grains also shows severe inhomogeneity. That

is, although Ta and Nb are nearly uniformly distributed in all nanocrystals, Mo and W preferentially co-enrich in some of the nanocrystals, while Ni preferentially enriches in other nanocrystals. The difference is that the Ni-rich particles are fewer in number, larger in size, and more dispersed spatially compared with the Mo-W-rich nanocrystals. These are likely to be Ni-rich secondary phases, which are expected to form since our designed Ni content (6 at.%) are above the solubility limits of four out of five binary systems. From the discussion above, it is clear that a complex bi-modal microstructure with severe compositional inhomogeneity was formed in n-HEA#1, featured by: (1) secondary clusters of grains decorated with randomly distributed Ni-rich and Mo-W-rich nanocrystals; (2) discrete domains containing Ti-rich patches and Ta-Nb-Ti-rich slabs. Fig. 1f shows an atomic-resolution HAADF-STEM image of the Ta-Nb-Ti rich slab obtained along the [001] zone axis. The spacing of the (110) plane of the Ta-Nb-Ti rich slab is determined as 0.237 nm, close to that of pure Ta (0.234 nm) or Nb (0.233 nm), indicating the slab has a similar but slightly distorted body-centered cubic (bcc) structure compared with pure Ta or Nb.

Figure 2a,b present representative HAADF-STEM images of the (TiNbMoTaW)-6Ni (n-HEA#2) sintered at 1400 °C. By correlating the EDS maps (Figs. 2c,e) at different scales to the microstructures (Figs. 2b,

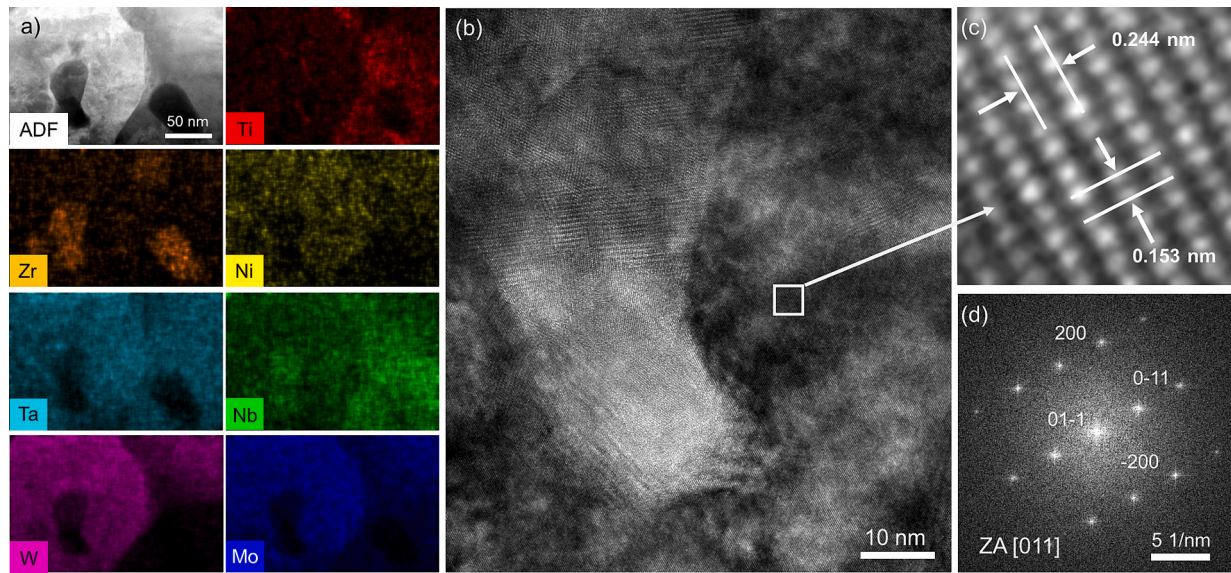


Fig. 6. Structure and chemistry of W-Mo-rich grains in n-HEA#3. (a,b) High-resolution EDS maps and HRTEM image of a W-Mo-rich grain. (c,d) Enlarged atomic-resolution image and corresponding fast Fourier transform (FFT) of the W-Mo-rich grain obtained along the [011] zone axis.

d), it is seen that the microstructure and chemical distribution of n-HEA#2 which is sintered at higher temperature are evidently different from n-HEA#1. Firstly, although the discrete Ti-rich patches still exist, their amount was considerably reduced. Secondly, the Ta-Nb-Ti-rich slabs are completely eliminated. Thirdly, the secondary-grain architecture in n-HEA#1 is eliminated, replaced by nearly uniformly distributed nanocrystals across the whole sample (except for the Ti-rich slabs). Note that, due to increased sintering temperature (from 1300 °C to 1400 °C), the average grain size (117 nm) of n-HEA#2 is slightly larger than that (95 nm) of n-HEA#1. Yet, the elemental distribution in these regions is still inhomogeneous (Fig. 2e, see another example in Fig. S5). Except for the Ti-rich patches, the Ta is nearly uniformly distributed across the sample, while Nb-Ti co-enrichment forms a continuous network, and Mo-W co-enrichment forms another continuous network. In contrast to the many differences, the configuration and distribution of the Ni-rich nanocrystals in n-HEA#2 are basically the same as that in n-HEA#1 (Figs. 2c,e). Figs. 3a-c show the bright-field STEM (BF-STEM) image and the overlapped EDS map of a Ti-rich patch. HRTEM and electron diffraction (Fig. 3c) show that the Ti-rich patch has a well-defined hexagonal close-packed (hcp) structure. Since the measured spacing of the (11-20) plane (0.25 nm) is larger than the 0.23 nm for pure Ti, it indicates that the a -axis of the Ti-rich phase is expanded compared with that of pure Ti.

Furthermore, the influence of alloying additions in tuning the alloy's structure and compositional inhomogeneity was further explored by adding Zr (5 at.%) into n-HEA#2. Fig. 4a presents a representative HAADF-STEM image of the n-HEA#3 specimen (see BF-STEM and HAADF-STEM images corresponding to the same region in Fig. S6). Statistical analysis shows that n-HEA#3 has an average grain size comparable to n-HEA#2 and n-HEA#1 (see details in Table S1). EDS maps (Fig. 4b) show that, although Nb-Ti co-enrichment and Mo-W co-enrichment (forming two different continuous networks) are still present, the microstructure and the compositional inhomogeneity of n-HEA#3 were evidently modified and is quite different from n-HEA#2. Firstly, with the addition of Zr, the size and the amount of the Ti-rich patches were both considerably reduced compared with that in both n-HEA#1 and n-HEA#2, and the refined Ti-rich nanocrystals distributed in a more disperse manner across the specimen; while, the size and distribution of the domains/networks formed by segregation of other elements (e.g. W, Mo, and Nb) remains almost the same (see statistics in Table S2). Secondly, the Ni in n-HEA#3 becomes nearly uniformly

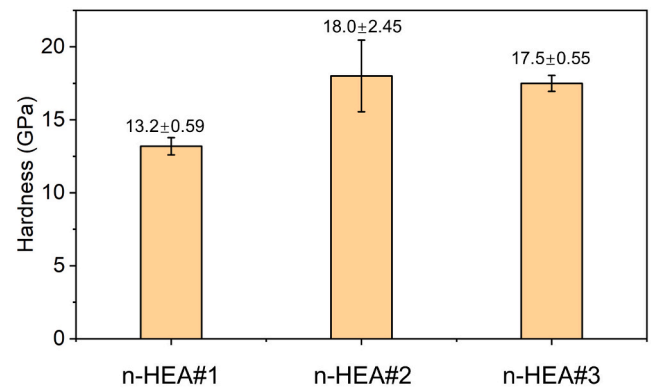


Fig. 7. Hardness of n-HEA#1, n-HEA#2, and n-HEA#3 by statistical nanoindentation tests. The hardness of n-HEA#1, n-HEA#2, and n-HEA#3 is determined to be 13.2 (± 0.59) GPa, 18.0 (± 2.45) GPa, and 17.5 (± 0.55) GPa, respectively, at the load force of 300 mN.

distributed, similar to Ta, indicating that the addition of Zr enhances the solubility of Ni in the alloy. Thirdly, although Zr improves the uniformity of the Ni distribution, preferential Zr segregation (the Zr-rich nanocrystals are randomly distributed across the sample) was observed in n-HEA#3 (Figs. 4b, 5a). By correlating high-resolution EDS to HRTEM imaging (Figs. 5b-d), we show that the Zr-rich nanocrystal has a (110) spacing of 0.25 nm which is basically the same as that of pure Zr. For the Mo-W-rich grains (Figs. 6a,b), according to the HRTEM image taken along the [011] zone axis, the (011) and (200) spacings are measured to be 0.244 nm and 0.153 nm (the corresponding values for bcc W are 0.226 nm and 0.159 nm, respectively). The $d_{(011)}/d_{(200)}$ ratio of 1.595 is evidently larger than the $d_{(011)}/d_{(200)}$ ratio of $\sqrt{2}$ for bcc W, indicating the atomic packing of the Mo-W-rich crystal deviates from the perfect bcc structure (Figs. 6c,d).

3.2. Hardness measurement

Statistical microstructural analysis and nanoindentation tests were further performed to understand the correlation between the alloys' chemical inhomogeneities and their mechanical properties. Fig. 7 shows the hardness of n-HEA#1, n-HEA#2, and n-HEA#3, which is determined

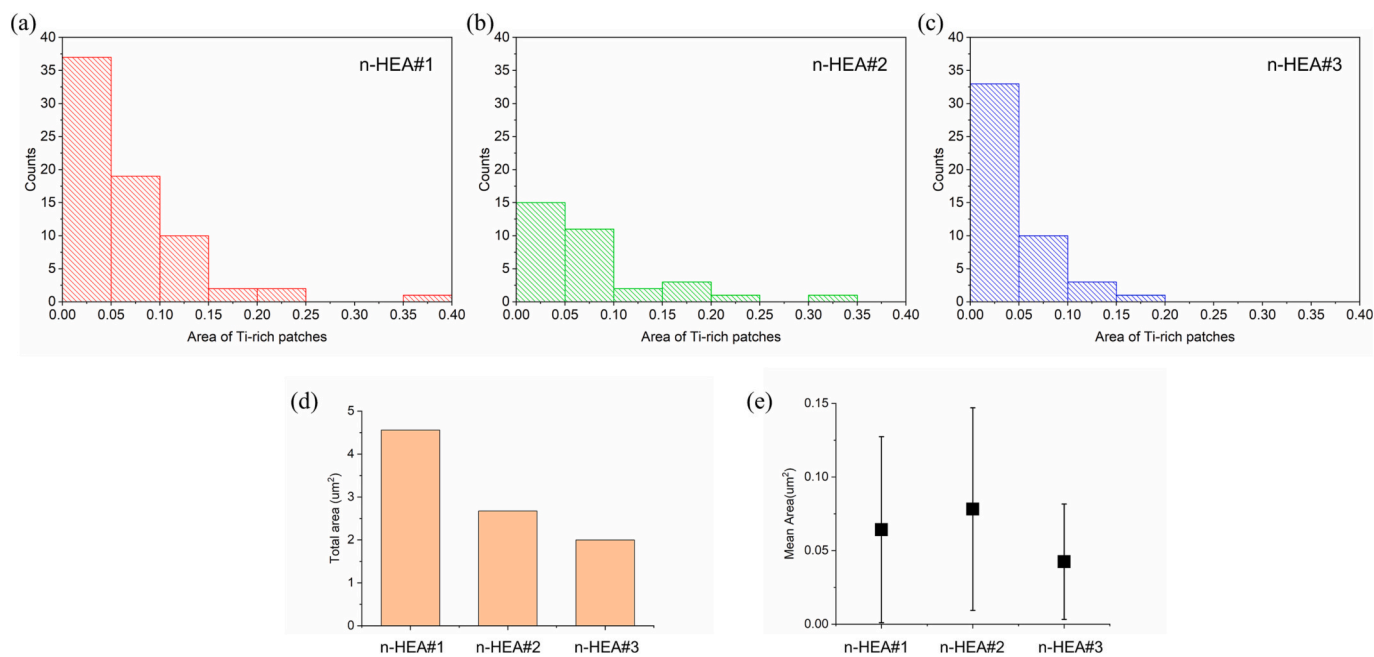


Fig. 8. Evolution of the compositional inhomogeneity in n-HEAs. (a-c) Histogram showing the size (area) distribution of the Ti-rich patches. (d) Area fraction of Ti-rich patches in n-HEAs. (e) Mean size (area) of the Ti-rich patches in n-HEAs.

to be 13.2 (± 0.59) GPa, 18.0 (± 2.45) GPa, and 17.5 (± 0.55) GPa, respectively, at the load force of 300 mN (see representative load-displacement curves of the three samples in Fig. S7). Fig. 8 shows statistical analysis of the evolution of the Ti-rich patches (the most evident compositional inhomogeneity arises from the Ti segregation). The histograms in Fig. 8a-c show that the amounts of Ti-rich patches with different sizes are all reduced from n-HEA#1 to n-HEA#2. Also, although the mean patch size increases slightly, the total area fraction of the Ti-rich patches is dramatically reduced by nearly one third, from 15.0% to 10.7% (Fig. 8d). Meanwhile, along with the reduced Ti-rich patches, the secondary-level architecture, that is, the aggregates of nanocrystals in n-HEA#1 are eliminated and replaced by uniformly distributed nanocrystals in n-HEA#2 (Note that the grain size of the nanocrystals in n-HEA#2 is slightly larger than that of n-HEA#1). The above factors are supposed to be the main contributors to the hardness increase (~ 5 GPa) of n-HEA#2 compared to that of n-HEA#1. Yet, despite the above benefits, one may notice that the hardness's standard deviation of n-HEA#2 is evidently larger than that of n-HEA#1. This is likely because, despite with larger size and amount, the spacing between discrete Ti-rich patches (430 ± 180 nm) within n-HEA#1 is generally smaller than the indentation width ($\sim 1.5 \mu\text{m}$), thus giving a relatively smaller standard deviation because the indenter always encounters Ti-rich patches in each indentation; in contrast, for n-HEA#2, although the amount of Ti-rich patches is reduced, their distribution becomes somewhat more localized (e.g., Ti-rich-patch-free regions with diameters larger than the indentation width can be identified in Fig. 2b).

4. Discussion

The observed increase in the uniformity of n-HEA#2 at a higher sintering temperature of 1400 °C, as compared to n-HEA#1 sintered at 1300 °C, can be attributed to several key changes in microstructure and elemental distribution. Firstly, the reduction of discrete Ti-rich patches in n-HEA#2 compared to n-HEA#1 is indicative of a more homogeneous dispersion of titanium within the alloy. Additionally, the elimination of Ta-Nb-Ti-rich slabs further contributes to the enhanced uniformity, as these structures are completely absent in n-HEA#2. Secondly, the sintering temperature increase has a remarkable impact on achieving a more uniform distribution of nanocrystals, indicated by the replacement

of the secondary-grain architecture in n-HEA#1 with nearly uniformly distributed nanocrystals throughout the entire sample in n-HEA#2. This change is crucial for improving the overall homogeneity of the alloy. Meanwhile, the elemental distribution in n-HEA#2, except for the Ti-rich patches, exhibits a higher level of uniformity. Therefore, despite the increase in sintering temperature leading to a slightly larger average grain size in n-HEA#2, the elimination of structural features such as discrete Ti-rich patches and Ta-Nb-Ti-rich slabs, coupled with the transition to a more uniformly distributed nanocrystal architecture, plays a crucial role in promoting uniformity within the alloy. This result suggests that higher temperatures facilitate the rearrangement of atoms, promoting a more homogeneous distribution of elements and contributing to the improved uniformity observed in n-HEA#2.

The comparison between n-HEA#3 and n-HEA#2 provides valuable insights into the effects of Zr addition on the microstructure and mechanical properties of the alloy. In particular, the examination reveals that, despite a reduction in Ti-rich patches in n-HEA#3 as compared to n-HEA#2, the alloy's hardness experiences a slight decrease. This unexpected trend is hypothesized to be a consequence of the composition change induced by the addition of Zr. While the decrease in hardness may be an initial concern, a closer inspection of the data uncovers a noteworthy improvement in the uniformity of the alloy. The standard deviation of the hardness of n-HEA#3 is significantly smaller (0.55 GPa) than that of n-HEA#2 (2.45 GPa), indicating a more uniform hardness distribution. This enhanced uniformity is attributed to two primary factors. Firstly, the Ti-rich patches in n-HEA#3 are not only reduced but also more finely distributed and refined. The size of these patches has been notably reduced, now comparable to the length scale of the nanocrystals. This reduction in patch size contributes to a more homogeneous mechanical properties throughout the sample. Secondly, the addition of Zr induces a redistribution of Ni within the alloy. In n-HEA#2, Ni is localized in a fraction of the nanocrystals. However, with Zr addition in n-HEA#3, Ni distribution becomes nearly uniform across all grains. This redistribution of Ni further enhances the homogeneity of the alloy's hardness, as each grain experiences a more even distribution of elements, resulting in a more consistent mechanical response.

5. Conclusions

In this work, we elucidate the influence of the sintering temperature and alloying on the compositional inhomogeneity and hardness of a model n-HEA, i.e., (TiNbMoTaW)6Ni, through coupled atomic-resolution TEM imaging, statistical chemical analysis, and nano-indentation tests. The main conclusions are summarized as follows:

- (1) Sintered at a relatively low temperature of 1300 °C, a complex bimodal microstructure (secondary grains and discrete patches) with severe compositional inhomogeneity forms in (TiNbMoTaW)6Ni.
- (2) With the sintering temperature increased to 1400 °C, the secondary-grain architecture (microsized aggregates of nanocrystals) transforms into uniformly distributed nanocrystals, the discrete Ti-rich patches are considerably reduced, and the Ta-Nb-Ti-rich slabs are completely eliminated.
- (3) When Zr is introduced into the n-HEA (sintered at 1400 °C), the microstructure and the compositional inhomogeneity can be further altered. Specifically, the size and the amount of the Ti-rich patches are considerably reduced. Moreover, due to the enhanced solubility of Ni induced by Zr alloying, the Ni distribution in the alloy becomes uniform, yet, Zr itself segregates in a manner similar to the Ni segregation in other n-HEAs.
- (4) Statistical microhardness tests show that the reduction of compositional inhomogeneity leads to higher hardness of the n-HEAs.

CRedit authorship contribution statement

Chunyang Wang: Data curation, Formal analysis, Investigation, Writing – original draft, Writing – review & editing, Validation, Visualization. **Mingde Qin:** Data curation, Investigation, Methodology. **Tianjiao Lei:** Data curation, Formal analysis, Investigation. **Liyang Wan:** Data curation, Investigation. **Sashank Shivakumar:** Investigation, Data curation. **Kim Kisslinger:** Data curation, Investigation. **Timothy J. Rupert:** Supervision, Writing – review & editing. **Jian Luo:** Supervision, Writing – review & editing. **Huolin L. Xin:** Conceptualization, Funding acquisition, Project administration, Supervision, Writing – review & editing.

Declaration of Competing Interest

The authors declare that they have no known competing financial interests or personal relationships that could have appeared to influence the work reported in this paper.

Data availability

Data will be made available on request.

Acknowledgements

This research was primarily supported by the National Science Foundation Materials Research Science and Engineering Center program through the UC Irvine Center for Complex and Active Materials (DMR-2011967). This work made use of the IMRI resources supported by the UCI and the UC Irvine MRSEC (DMR-2011967) and resources supported by the Center for Functional Nanomaterials, which is a U.S. DOE Office of Science Facility, at Brookhaven National Laboratory under Contract No. DE-SC0012704.

Appendix A. Supplementary data

Supplementary data to this article can be found online at <https://doi.org/10.1016/j.matchar.2023.113563>.

References

- [1] B. Cantor, I.T.H. Chang, P. Knight, A.J.B. Vincent, Microstructural development in equiatomic multicomponent alloys, *Mater. Sci. Eng. A* 375–377 (2004) 213–218.
- [2] J.-W. Yeh, S.-J. Lin, T.-S. Chin, J.-Y. Gan, S.-K. Chen, T.-T. Shun, C.-H. Tsau, S.-Y. Chou, Formation of simple crystal structures in Cu-Co-Ni-Cr-Al-Fe-Ti-V alloys with multiprincipal metallic elements, *Metall. Mater. Trans. A* 35 (8) (2004) 2533–2536.
- [3] J.W. Yeh, S.K. Chen, S.J. Lin, J.Y. Gan, T.S. Chin, T.T. Shun, C.H. Tsau, S.Y. Chang, Nanostructured high-entropy alloys with multiple principal elements: novel alloy design concepts and outcomes, *Adv. Eng. Mater.* 6 (5) (2004) 299–303.
- [4] Y.P. Cai, G.J. Wang, Y.J. Ma, Z.H. Cao, X.K. Meng, High hardness dual-phase high entropy alloy thin films produced by interface alloying, *Scr. Mater.* 162 (2019) 281–285.
- [5] Q. Pan, M. Yang, R. Feng, A.C. Chuang, K. An, P.K. Liao, X. Wu, N.R. Tao, L. Lu, Atomic faulting induced exceptional cryogenic strain hardening in gradient cell-structured alloy, *Science* 382 (2023) 185–190.
- [6] J.Y. He, H. Wang, H.L. Huang, X.D. Xu, M.W. Chen, Y. Wu, X.J. Liu, T.G. Nieh, K. An, Z.P. Lu, A precipitation-hardened high-entropy alloy with outstanding tensile properties, *Acta Mater.* 102 (2016) 187–196.
- [7] R. Chen, G. Qin, H. Zheng, L. Wang, Y. Su, Y. Chiu, H. Ding, J. Guo, H. Fu, Composition design of high entropy alloys using the valence electron concentration to balance strength and ductility, *Acta Mater.* 144 (2018) 129–137.
- [8] J. Pang, H. Zhang, L. Zhang, Z. Zhu, H. Fu, H. Li, A. Wang, Z. Li, H. Zhang, A ductile Nb40Ti25Al15V10Ta5Hf3W2 refractory high entropy alloy with high specific strength for high-temperature applications, *Mater. Sci. Eng. A* 831 (2022) 142290.
- [9] T. Xiong, S. Zheng, J. Pang, X. Ma, High-strength and high-ductility AlCoCrFeNi2.1 eutectic high-entropy alloy achieved via precipitation strengthening in a heterogeneous structure, *Scr. Mater.* 186 (2020) 336–340.
- [10] Z. Yu, B. Xie, Z. Zhu, B. Xu, M. Sun, High-temperature deformation behavior and processing maps of a novel AlNbTi3VZr1.5 refractory high entropy alloy, *J. Alloys Compd.* 912 (2022) 165220.
- [11] Z. Li, K.G. Pradeep, Y. Deng, D. Raabe, C.C. Tasan, Metastable high-entropy dual-phase alloys overcome the strength-ductility trade-off, *Nature* 534 (7606) (2016) 227–230.
- [12] P. Cao, Maximum strength and dislocation patterning in multi-principal element alloys, *Sci. Adv.* 8 (45) (2022) eabq7433.
- [13] J. Wang, S. Wu, S. Fu, S. Liu, M. Yan, Q. Lai, S. Lan, H. Hahn, T. Feng, Ultrahigh hardness with exceptional thermal stability of a nanocrystalline CoCrFeNiMn high-entropy alloy prepared by inert gas condensation, *Scr. Mater.* 187 (2020) 335–339.
- [14] R. Feng, Y. Rao, C. Liu, X. Xie, D. Yu, Y. Chen, M. Ghazisaeidi, T. Ungar, H. Wang, K. An, P.K. Liaw, Enhancing fatigue life by ductile-transformable multicomponent B2 precipitates in a high-entropy alloy, *Nat. Commun.* 12 (1) (2021) 3588.
- [15] R. Feng, C. Zhang, M.C. Gao, Z. Pei, F. Zhang, Y. Chen, D. Ma, K. An, J. D. Poplawsky, L. Ouyang, Y. Ren, J.A. Hawk, M. Widom, P.K. Liaw, High-throughput design of high-performance lightweight high-entropy alloys, *Nat. Commun.* 12 (1) (2021) 4329.
- [16] Q. Pan, L. Zhang, R. Feng, Q. Lu, K. An, A.C. Chuang, J.D. Poplawsky, P.K. Liaw, L. Lu, Gradient cell-structured high-entropy alloy with exceptional strength and ductility, *Science* 374 (6570) (2021) 984–989.
- [17] L.S. Mantha, B.E. MacDonald, X. Mu, A. Mazilkin, J. Ivanisenko, H. Hahn, E. J. Lavernia, S. Katmagallu, C. Kübel, Grain boundary segregation induced precipitation in a non equiatomic nanocrystalline CoCuFeMnNi compositionally complex alloy, *Acta Mater.* 220 (2021) 117281.
- [18] Q. Ding, Y. Zhang, X. Chen, X. Fu, D. Chen, S. Chen, L. Gu, F. Wei, H. Bei, Y. Gao, M. Wen, J. Li, Z. Zhang, T. Zhu, R.O. Ritchie, Q. Yu, Tuning element distribution, structure and properties by composition in high-entropy alloys, *Nature* 574 (7777) (2019) 223–227.
- [19] X. Chen, Q. Wang, Z. Cheng, M. Zhu, H. Zhou, P. Jiang, L. Zhou, Q. Xue, F. Yuan, J. Zhu, X. Wu, E. Ma, Direct observation of chemical short-range order in a medium-entropy alloy, *Nature* 592 (7856) (2021) 712–716.
- [20] R. Zhang, S. Zhao, J. Ding, Y. Chong, T. Jia, C. Ophus, M. Asta, R.O. Ritchie, A. M. Minor, Short-range order and its impact on the CrCoNi medium-entropy alloy, *Nature* 581 (7808) (2020) 283–287.
- [21] H.W. Hsiao, R. Feng, H. Ni, K. An, J.D. Poplawsky, P.K. Liaw, J.M. Zuo, Data-driven electron-diffraction approach reveals local short-range ordering in CrCoNi with ordering effects, *Nat. Commun.* 13 (1) (2022) 6651.
- [22] Y. Li, Y. Wei, Z. Wang, X. Liu, T. Colnaghi, L. Han, Z. Rao, X. Zhou, L. Huber, R. Dsouza, Y. Gong, J. Neugebauer, A. Marek, M. Rampp, S. Bauer, H. Li, I. Baker, L. Stephenson, B. Gault, Quantitative three-dimensional imaging of chemical short-range order via machine learning enhanced atom probe tomography, *Nat. Commun.* 14 1 (2023) 7410.
- [23] C. Zhang, H. Wang, X. Wang, Y.T. Tang, Q. Yu, C. Zhu, M. Xu, S. Zhao, R. Kou, X. Wang, B.E. MacDonald, R.C. Reed, K.S. Vecchio, P. Cao, T.J. Rupert, E. J. Lavernia, Strong and ductile refractory high-entropy alloys with super formability, *Acta Mater.* 245 (2023) 118602.
- [24] S. Kumar, A. Linda, Y. Shadangi, V. Jindal, Influence of micro-segregation on the microstructure, and microhardness of MoNbTaTi(1-x)W refractory high entropy alloys: experimental and DFT approach, *Intermetallics* 164 (2024) 108080.
- [25] P. Kumar, S.J. Kim, Q. Yu, J. Ell, M. Zhang, Y. Yang, J.Y. Kim, H.-K. Park, A. M. Minor, E.S. Park, R.O. Ritchie, Compressive vs. tensile yield and fracture toughness behavior of a body-centered cubic refractory high-entropy superalloy Al0.5Nb1.25Ta1.25TiZr at temperatures from ambient to 1200°C, *Acta Mater.* 245 (2023) 118620.

- [26] V.K. Pandey, Y. Shadangi, V. Shivam, B.N. Sarma, N.K. Mukhopadhyay, Theoretical and experimental study on phase stability of TiVZrMoW refractory high entropy alloy, *Philos. Mag.* 102 (6) (2021) 480–503.
- [27] A. Roh, D. Kim, S. Nam, D.-I. Kim, H.-Y. Kim, K.-A. Lee, H. Choi, J.-H. Kim, NbMoTaW refractory high entropy alloy composites strengthened by in-situ metal-non-metal compounds, *J. Alloys Compd.* 822 (2020) 153423.
- [28] O.N. Senkov, G.B. Wilks, J.M. Scott, D.B. Miracle, Mechanical properties of Nb₂₅Mo₂₅Ta₂₅W₂₅ and V₂₀Nb₂₀Mo₂₀Ta₂₀W₂₀ refractory high entropy alloys, *Intermetallics* 19 (5) (2011) 698–706.
- [29] O.A. Waseem, H.J. Ryu, Powder metallurgy processing of a W(x)TaTiVCr high-entropy alloy and its derivative alloys for fusion material applications, *Sci. Rep.* 7 (1) (2017) 1926.
- [30] K. Xun, B. Zhang, Q. Wang, Z. Zhang, J. Ding, E. Ma, Local chemical inhomogeneities in TiZrNb-based refractory high-entropy alloys, *J. Mater. Sci. Technol.* 135 (2023) 221–230.
- [31] Q. Liu, G. Wang, X. Sui, Y. Liu, X. Li, J. Yang, Microstructure and mechanical properties of ultra-fine grained MoNbTaTiV refractory high-entropy alloy fabricated by spark plasma sintering, *J. Mater. Sci. Technol.* 35 (11) (2019) 2600–2607.
- [32] J.J. Jasinski, T. Stasiak, W. Chmurzynski, L. Kurpaska, M. Chmielewski, M. Frelek-Kozak, M. Wilczopolska, K. Mulewska, M. Zielinski, M. Kowal, R. Diduszko, W. Chrominski, J. Jagielski, Microstructure and phase investigation of FeCrAl-Y₂O₃ ODS steels with different Ti and V contents, *J. Nucl. Mater.* 586 (2023) 154700.
- [33] A. Olejarczyk, W.Y. Huo, M. Zieliński, R. Diduszko, E. Wyszowska, A. Kosińska, D. Kalita, I. Józwiak, M. Chmielewski, F. Fang, L. Kurpaska, Microstructure and mechanical properties of mechanically-alloyed CoCrFeNi high-entropy alloys using low ball-to-powder ratio, *J. Alloys Compd.* 938 (2023) 168196.
- [34] D. Kalita, I. Józwiak, L. Kurpaska, Y. Zhang, K. Mulewska, W. Chrominski, J. O'Connell, Y. Ge, W.L. Boldman, P.D. Rack, Y. Wang, W.J. Weber, J. Jagielski, The microstructure and He⁺ ion irradiation behavior of novel low-activation W-Ta-Cr-V refractory high entropy alloy for nuclear applications, *Nucl. Mater. Energy* 37 (2023) 101513.
- [35] M. Qin, S. Shivakumar, J. Luo, Refractory high-entropy nanoalloys with exceptional high-temperature stability and enhanced sinterability, *J. Mater. Sci.* 58 (20) (2023) 8548–8562.
- [36] Y. Tong, L. Bai, X. Liang, Y. Chen, Z. Zhang, J. Liu, Y. Li, Y. Hu, Influence of alloying elements on mechanical and electronic properties of NbMoTaWX (X = Cr, Zr, V, Hf and re) refractory high entropy alloys, *Intermetallics* 126 (2020) 106928.